AFRL-RX-WP-TR-2010-4189

COLLABORATIVE RESEARCH AND DEVELOPMENT (CR&D)
Task Order 0049: Tribological Modeling

Young Sup Kang

Universal Technology Corporation

MAY 2008
Final Report

STINFO COPY

AIR FORCE RESEARCH LABORATORY
MATERIALS AND MANUFACTURING DIRECTORATE
WRIGHT-PATTERSON AIR FORCE BASE, OH 45433-7750
AIR FORCE MATERIEL COMMAND
UNITED STATES AIR FORCE

NOTICE AND SIGNATURE PAGE

This report was cleared for public release by the USAF 88th Air Base Wing (88 ABW) Public Affairs Office (PAO) and is available to the general public, including foreign nationals. Copies may be obtained from the Defense Technical Information Center (DTIC) (http://www.dtic.mil).

AFRL-RX-WP-TR-2010-4189 HAS BEEN REVIEWED AND IS APPROVED FOR PUBLICATION IN ACCORDANCE WITH THE ASSIGNED DISTRIBUTION STATEMENT.

*//Signature//   //Signature//

_____   _____
MARK GROFF   KENNETH A. FEESER
Program Manager   Branch Chief
Business Operations Branch   Business Operations Branch
Materials & Manufacturing Directorate   Materials & Manufacturing Directorate

REPORT DOCUMENTATION PAGE

Form Approved
OMB No. 0704-0188

1. REPORT DATE *(DD-MM-YY)*	2. REPORT TYPE	3. DATES COVERED *(From - To)*
May 2008	Final	01 July 2006 – 01 May 2008

4. TITLE AND SUBTITLE
COLLABORATIVE RESEARCH AND DEVELOPMENT (CR&D)
Task Order 0049: Tribological Modeling

5a. CONTRACT NUMBER
F33615-03-D-5801-0049

5b. GRANT NUMBER

5c. PROGRAM ELEMENT NUMBER
62102F

6. AUTHOR(S)
Young Sup Kang

5d. PROJECT NUMBER
4349

5e. TASK NUMBER
L0

5f. WORK UNIT NUMBER
4349L0VT

7. PERFORMING ORGANIZATION NAME(S) AND ADDRESS(ES)
Universal Technology Corporation
1270 North Fairfield Road
Dayton, OH 45432-2600

8. PERFORMING ORGANIZATION REPORT NUMBER
S-531-049

9. SPONSORING/MONITORING AGENCY NAME(S) AND ADDRESS(ES)
Air Force Research Laboratory
Materials and Manufacturing Directorate
Wright-Patterson Air Force Base, OH 45433-7750
Air Force Materiel Command
United States Air Force

10. SPONSORING/MONITORING AGENCY ACRONYM(S)
AFRL/RXOB

11. SPONSORING/MONITORING AGENCY REPORT NUMBER(S)
AFRL-RX-WP-TR-2010-4189

12. DISTRIBUTION/AVAILABILITY STATEMENT
Approved for public release; distribution unlimited.

13. SUPPLEMENTARY NOTES
PAO Case Number: 88ABW 2010-1231; Clearance Date: 17 Mar 2010. Report contains color.

14. ABSTRACT

This research in support of the Air Force Research Laboratory Materials and Manufacturing Directorate was conducted at Wright-Patterson AFB, Ohio from 1 July 2006 - 1 May 2008. This task worked to develop and validate models for tribological interfaces to provide guidance to the materials development R&D activities of AFRL/RXBT. Nanocomposite tribological coatings have been developed for the better performance and longer service life of machine components in extreme environments due to the improvement of the hardness, toughness, wear resistance, and friction reduction. Nanocomposite coatings consist of nanocrystalline phases encapsulated into an amorphous matrix for the optimum mechanical performance and load support.

A finite element analysis (FEA) model was developed to investigate the behavior of nanocomposite coatings due to the nanoindentation. The concept of Voronoi tessellation has been used to model the geometrical features of random microstructure for the nanocomposite coatings. The FEA model was used for the study of stress distribution and deformation of nanocomposite coatings under the nanoindentation. Also, the FEA model was used for the design optimization of nanocomposite coating with different combination of crystalline phases and amorphous matrices for the various contact conditions

15. SUBJECT TERMS
tribological modeling

16. SECURITY CLASSIFICATION OF:			17. LIMITATION OF ABSTRACT:	18. NUMBER OF PAGES	19a. NAME OF RESPONSIBLE PERSON (Monitor)
a. REPORT	**b. ABSTRACT**	**c. THIS PAGE**	SAR	32	Mark Groff
Unclassified	Unclassified	Unclassified			19b. TELEPHONE NUMBER *(Include Area Code)* N/A

Standard Form 298 (Rev. 8-98)
Prescribed by ANSI Std. Z39-18

i

Introduction

Wear protective coatings have been developed to protect the contacting surfaces from friction and wear. The design architecture and composition of the coatings should consider the operating environments as a main design factor to maintain the tribological performance of coatings. Although a typical material has a limited operating range to maintain its best tribological performance, the nanocomposite coating design provides the multi-functionalities such as high hardness, high toughness, and low friction to one coating system for wide operating ranges. Previous developments on nanocomposite coatings show the improvement of hardness, toughness, friction reduction and wear resistance under severe operating conditions [1-8]. One of the nanocomposite design concepts is that nanocrystalline phases are encapsulated into an amorphous matrix because nanocrystalline phases with strong interaction with matrix phase provide superhardness. Veprek et al. [2] proposed a nanocomposite design concept based on avoiding dislocation formation and blocking the crack propagation in a 0.3 – 0.5 nm thin amorphous tissue. Also, Veprek and Argon [3] suggested an optimal nanocomposite grain size, 3 – 5 nm, based on the interatomic bond distance.

Yttria-stabilized-zirconia (YSZ) has a unique property combination that makes YSZ be an excellent candidate for a thin film to protect metal and alloy surfaces from high temperature environment, erosion and wear. However, since a ceramic is a very brittle material, YSZ films easily experience cracking when the deformation is beyond the elastic limit of the YSZ material. To improve the toughness and brittleness of oxide ceramic films, nanocomposite coatings with YSZ and gold were developed [4]. The combination of nanocrystalline phases and amorphous matrix improved the toughness while maintaining the high hardness and elastic modulus. Also, YSZ in a gold matrix was developed with encapsulated nanosized reservoirs of MoS_2 and diamondlike carbon (DLC) [1] because of the outstanding performance at high temperature. Furthermore, Voevodin et al. [1] proposed a "chameleon design concept" for YSZ/Au/MoS_2/DLC and WC/DLC/WS nanocomposite coatings because of the unique coating skin adaptation, that is, "Chameleon" nanocomposite coatings show the reversible adaptability to humidity or temperature. "Chameleon" nanocomposite coatings were developed for the extremely changing environments from earth atmosphere to space by the self-adjusting surface tribological properties to maintain the performance, that is, the coating friction surface changes its chemistry and structure depending on the operating environments. It was found that the mechanical properties of the nanocomposite coatings such as WC/WS_2/DLC and YSZ/Au/MoS_2/DLC exhibit a very strong dependence on coating composition [1].

Contact problems of the coated surfaces have been modeled by many researchers [9 – 14] using finite element analysis (FEA) technique. Most of the coatings investigated are single or multilayered coating systems. These studies were focused on the elastic or elastic-plastic behavior of the coating system and subsequent stress distribution under the Hertzian contact conditions. Parametric studies show the effects of critical design parameters such as contact width, friction coefficient, stiffness of layer, and etc. on the stress distribution and deformation inside the coating system. Coating parameter effects on the initiation and propagation of plastic zone for TiN/Ti coating system had been investigated using FEA models [9,10]. FEA model was developed to study the deformation associated with indentation of coating system [11]. The elastic compliance of the coating system was determined as a function of the indentation depth from the load-displacement curve. The stress-strain relationship between the substrate strength

and layer thickness was studied on TiN coating system and the consequent effect on the load capacity was investigated [12]. Gorishnyy and Olson [15] developed a FEA model to investigate the distribution of stress in single layer, bi-layer and multilayer films under combined normal and tangential loads. Recently, Veprek et al. [16] developed a new method for FEA modeling of ultra-hard ceramic coating indentations. Bull [17] repeated the FEA modeling of the scratch test for TiN on stainless steel with better substrate mechanical properties.

This present study was focused on the study of stress distribution and elastic-plastic deformation on the nanocomposite coating systems developed at the Air Force Research Laboratory (RXBT). The FEA technique has been applied to the nanocomposite coating system model due to the nonlinear nature of the coating system behavior using commercial softwares such as ABAQUS/CAE and ABAQUS/Standard. The FEA model has been used to understand the mechanisms involved in tribological contacts for a wide range of material properties, compositions, and applied loads. Ultimately, this study will provide a design guideline for nanocomposite coatings.

Nanocomposite Tribological Coating

Voevodin et al. [1] illustrated the need for the nanocomposite coatings in extreme environments and developed the nanocomposite coating system shown in Figures 1 (a) and 1 (b). Figure 1(a) shows the schematic of nanocomposite coating system, featuring a crystalline/amorphous design in the main coating layer for cohesive toughness and a functionally gradient interface layer for adhesive toughness. It shows the nanocomposite coating, substrate, and gradient interface to enhance the adhesion strength and relieve interface stresses. Figure 1(b) depicts the schematic of nanocomposite coating design structure, that is, an amorphous matrix and crystalline phase (YSZ) were used for an optimum mechanical performance and load support. This nanocomposite has 3 - 10 nm crystalline grains in an amorphous matrix. The grains are separated by an amorphous matrix with 1 - 3 nm. This crystalline grain size is for the optimal hardness and toughness [1,3]. Also, this design was used to produce the optimum tribological performance.

Figure 2 shows HRTEM (high resolution transmission electron microscope) image and SAD (submicron selected area electron diffraction) pattern obtained from $(YSZ)_{0.48} Au_{0.12}$ $(MoS_2)_{0.18} C_{0.22}$, that is, an example of "Chameleon" nanocomposite coating produced by a hybrid of laser ablation and magnetron sputtering [1]. The SAD pattern of $(YSZ)_{0.48} Au_{0.12}$ $(MoS_2)_{0.18} C_{0.22}$ nanocomposite coating demonstrates the rings for tetragonal ZrO_2 as well as face centered cubic Au and the diffused halo for amorphous carbon. Dark regions correspond to Au and YSZ nanocrystallines while bright regions correspond to amorphous matrix. The size of YSZ crystalline is 3-5 nm for the optimal load support and stability [3]. The size of Au crystalline is 3 - 8 nm for the high temperature lubricant. The carbon and MoS_2 are amorphous for the ambient lubrication and the space lubrication, respectively. The initial model was proposed and explained by [5,6]. The dislocation formation is restricted in small grains (3 – 5nm) and the strength of nanocrystals approaches the ideal one that is of the order of about 10 % of the shear modulus.

Finite Element Analysis Approach

Figures 3 (a) and 3 (b) show the schematic of line contact for nanocomposite coating system and its corresponding finite element analysis model. The two-dimensional line contact finite element analysis (FEA) model is to analyze contact stress distribution in nanocomposite

coating system generated by a rigid cylindrical indenter. The commercial finite element softwares such as ABAQUS/CAE and ABAQUS/Standard were used to model the coating system under the plane-strain assumption. To reduce the computing time, the relatively coarse mesh was used for the region far away from the contact zone. Very fine mesh was used for the nanocomposite coating adjacent to the coating/rigid indenter interface near the contact zone in order to determine the stress distribution and deformation field accurately. Nearly 127671 nodes and 253331 elements were used to model the entire system. The three-node linear plain strain element (CPE3) was used. Coulomb friction was used to model the contact between the top coating surface and the rigid indenter. Due to the perfect bonding assumptions, the continuous displacement at the grain-matrix interfaces, coating interfaces, and coating/substrate interface is applied. Since the strain hardening is not considered, elastic perfectly plastic stress-strain relationships were used for the gradient coating materials and the substrate material. The onset of plastic yield begins by the von Mises yield criterion for the isotropic materials. Figure 3(b) demonstrates the von Mises stress distribution inside the nanocomposite coating system generated by a rigid indenter. Please note that the residual compressive stresses associated with the process of deposition are negligible because the nanocomposite coating thickness is a few micros. Nanocomposite coating system design incorporating functionally gradient interfaces with nanocomposites provide significant improvement of the tribological properties [7]. The design suggests the small size hard crystalline grains surrounded by an amorphous matrix to stop crack propagation. Grain boundary sliding improves the ductility of the nanocomposite coatings.

Figures 4 (a) and 4 (b) show the two dimensional random microstructure geometries generated based on the concept of Voronoi tessellation. A Voronoi tessellation represents a cell structure constructed from a Poisson point process by introducing planar cell walls perpendicular to lines connecting neighboring points. This results in a set of convex polygons embedding the points and their domains of attraction, which completely fill up the underlying space. The concept of Voronoi tessellation has recently been extensively used in material science, especially to model random microstructures like aggregates of grains in polyscrystals, patterns of intergranular cracks, and composites [18]. Figures 4 (a) and 4 (b) have been generated by using MATLAB. The RAND command produces pseudo-random numbers [19]. The sequence of numbers generated is determined by the state of the generator. Figure 4 (a) was generated by resetting the generator to its 75th state while figure 4(b) was generated by resetting the generator to its 50th state.

Figure 5 depicts the finite element analysis model developed for nanocomposite coating system nanoindentation. The coating system consists of nanocomposite coating, gradient interface, and substrate. Figure 5 clearly demonstrates the random geometrical structure of nanocomposite coating and functionally gradient interface generated using ABAQUS/CAE. The enlarged view shows the combination of crystalline phase/amorphous matrix structure. Table 1 shows the mechanical material properties of $YSZ/Au/MoS_2/DLC$ composite coatings [1]. Coating hardness and modulus of elasticity were evaluated using nanoindentation. The results show that the nanocomposite composition and deposition temperature play important roles for improving the hardness and modulus of elasticity of the coating. The hardness of the YSZ/Au coatings decreases with the addition of MoS_2 and, to a less extent, carbon.

Yield Strength Calculation Procedure

To develop the elastic-perfectly plastic FEA model for nanocomposite coating system with functionally gradient Ti/TiC interface, the yield strengths of thin interface materials should

3

be obtained. Although there are no measured yield strength results from nanoindentation experiments, by the aid of the numerical nanoindentation simulation using a FEA model, the yield strengths of thin interfaces are able to be calculated. Therefore, an interactive procedure between FEA model simulations and nanoindentation experiments is required to calculate the yield strengths of the thin interface materials. It is assumed that the plastic deformation of an interface material is initiated when its von Mises stress generated inside the interface block becomes greater than yield strength of the interface material.

The measured modulus of elasticity of the interface material is used as an input parameter to the FEA model for the nanoindentation simulation. Since yield strength of the interface material is required as an input parameter for the nanoindentation simulation, the initial yield strength of the interface material is estimated based on the measured hardness value of the material, i.e., one third of the hardness. Then, the numerical load vs. displacement curve is generated using the initial estimated yield strength and the measured modulus of elasticity. If the loading and unloading parts of the load vs. displacement curve show the discrepancy between the experimental and numerical curves, the second numerical load vs. displacement curve is needed to be obtained with either reduced or increased estimated yield strength. The slope of the second numerical load vs. displacement curve indicates the magnitude of the next estimated yield strength value. This step requires an iterative procedure to obtain a best-fit load vs. displacement curve from the nanoindentation simulation by changing the yield strength input parameter value for the simulation. Therefore, when the computational best-fit load vs. displacement curve matches the experimental averaged load vs. displacement curve closely, the estimated yield strength value is considered as the yield strength of the material. Please note that the yield strength of each material is determined from the nanoindentation simulation.

Results and Discussion

The experimental results for $Ti_{.53}C_{.47}$ interface from nanoindentation are shown in Figures 6(a) through 6 (d). The indentation depth to $Ti_{.53}C_{.47}$ interface sample is limited to 100 nm to avoid the substrate effect on measured material properties. Figure 6(a) shows scattered data for hardness vs. displacement curves because of the surface roughness effect on the measurement. The hardness increases as the nanoindentation depth increases for $Ti_{.53}C_{.47}$ interface. The average hardness increases as the nanoindentation depth increases for $Ti_{.53}C_{.47}$ interface. The average hardness of $Ti_{.53}C_{.47}$ interface from the nanoindentation experiments is 14.2 ± 1.8 GPa. The thick solid line represents the average hardness value of $Ti_{.53}C_{.47}$ interface along the indentation depth. Figure 6(b) depicts the modulus of elasticity vs. displacement curves for $Ti_{.53}C_{.47}$ interface. The average modulus of elasticity of $Ti_{.53}C_{.47}$ interface is 231.1 ± 34.6 GPa. The thick solid line shows the average value of the modulus of elasticity for $Ti_{.53}C_{.47}$ interface along the indentation depth. Figure 6(c) illustrates the load vs. displacement curves for $Ti_{.53}C_{.47}$ interface from nanoindentation. Due to the roughness of surface, the data is scattered. Figure 6(d) shows the comparison of averaged experimental results and best-fit FEA results for $Ti_{.53}C_{.47}$ interface. The average load vs. displacement curve agrees well with best-fit load vs. displacement curve when Y = 10 GPa and E = 240 GPa are used for $Ti_{.53}C_{.47}$ interface nanoindentation simulation.

Figure 7 demonstrates the schematic of functionally gradient (FG) Ti/TiC interface design with programmed variation of compositional and mechanical properties proposed by Voevodin et al. [20]. Each layer has its unique material properties and thickness. Hardness and modulus of elasticity of Ti/TiC interface system are measured from interface samples. 25

indentation locations per sample were averaged to obtain the statistical values. The yield strength for each interface material is calculated from FEA nanoindentation simulation using the measured hardness and modulus of elasticity. These are the values used for inputs to FEA nanocomposite coating system model for this study. The material properties of each layer were linearly interpolated from the measured material properties data. To improve adhesion between the substrate and upper carbide layers, α-Ti is used as a bond layer.

The FEA model was used to evaluate; (1) the effect of different crystalline phases such as YSZ and MoS_2 in amorphous YSZ/Au matrix on the von Mises stress distribution; (2) the effect of different amorphous YSZ/Au matrix compositions on the von Mises stress distribution as YSZ crystalline phase molar % increases; and (3) the effect of different crystalline phase densities such as 20 Vol. % and 75 Vol. % (Volume %) in amorphous YSZ/Au matrix on the von Mises stress distribution. Figures 8 (a) through 8(d) show the contour plots of von Mises stress distribution inside the nanocomposite coating system indented by a rigid cylindrical indenter in order to study the effect of different crystalline phase properties on von Mises stress distribution inside the different nanocomposite coatings such as $YSZ_{.71}Au_{.11}YSZ$, $YSZ_{.71}Au_{.11}MoS_2$, $YSZ_{.58}Au_{.18}YSZ$, and $YSZ_{.58}Au_{.18}MoS_2$. Figures 8 (a) through 8 (d) illustrate that the von Mises stress field below the surface varies as the crystalline phase and YSZ/Au matrix composition are changed with indentation depth = 7 nm and friction coefficient, 0.0. Please note that the maximum von Mises stress always occurs at certain depth along the axis of depth below the center of the contact. Figure 8 (a) is the contour plot of von Mises stress for $YSZ_{.71}Au_{.11}YSZ$ nanocomposite coating with a normal displacement, $\delta = 7$ nm. The maximum von Mises stress occurs inside the $YSZ_{.71}Au_{.11}YSZ$ coating system with the magnitude of 2.28 GPa. The YSZ crystalline phase exhibits the highest von Mises stress because of the higher modulus of elasticity than $YSZ_{.71}Au_{.11}$ matrix. With the MoS_2 crystalline phase, the maximum von Mises stress occurs below the contact surface with the magnitude of 1.90 GPa inside the $YSZ_{.71}Au_{.11}$ amorphous matrix. Figure 8 (c) shows the contour plot of von Mises stress for $YSZ_{.58}Au_{.18}YSZ$ with a normal displacement, $\delta = 7$ nm. The maximum von Mises stress occurs with the magnitude of 2.27 GPa. Figure 8 (d) shows the contour plot of von Mises stress for $YSZ_{.58}Au_{.18}MoS_2$ with a normal displacement, $\delta = 7$ nm. The maximum von Mises stress occurs with the magnitude of 1.90 GPa. Note that there are vertical lines on the contour plot of von Mises stress distribution inside the nanocomposite coating because of the repeated duplication of the small nanocomposite structure pattern. In general, $YSZ_{.71}Au_{.11}YSZ$ nanocomposite coating generates higher von Mises stress distribution than $YSZ_{.71}Au_{.11}MoS_2$ nanocomposite coating under the same loading conditions because of the higher Young's modulus of YSZ crystalline phase. $YSZ_{.71}Au_{.11}YSZ$ nanocomposite coating has slightly higher von Mises stress than $YSZ_{.58}Au_{.18}YSZ$ nanocomposite coating because $YSZ_{.71}Au_{.11}$ amorphous matrix has higher Young's modulus than $YSZ_{.58}Au_{.18}$ matrix. Table 2 shows the material property values used for the FEA model [8].

Figures 9 (a) through 9 (d) show the contour plots of the von Mises stress distribution for YSZ/Au/MoS_2 nanocomposite coatings with different amorphous matrix compositions to represent the effect of amorphous matrix composition properties on Von Mises stress distribution. Figure 9(a) depicts the contour plot of von Mises stress distribution inside $YSZ_{.65}Au_{.35}MoS_2$ nanocomposite coating system with the indentation depth of 7 nm with maximum von Mises $\sigma_{max} = 1.27$ GPa. The maximum von Mises stress occurs YSZ/Au amorphous matrix region because of the higher Young's modulus of YSZ/Au matrix. Figures 9(b) through 9(d) show the contour plot of von Mises stress distribution inside $YSZ_{.75}Au_{.25}MoS_2$ nanocomposite coating

5

with the maximum von Mises stress, σ_{max} = 1.83 GPa, YSZ$_{.85}$Au$_{.15}$MoS$_2$ with σ_{max} = 2.22 GPa, and YSZ$_{.95}$Au$_{.5}$MoS$_2$ with σ_{max} = 2.59 GPa, respectively. In general, the hardness and young's modulus of YSZ/Au matrix increases as the YSZ composition increases in YSZ/Au matrix. Therefore, the YSZ$_{.95}$Au$_{.5}$MoS$_2$ nanocomposite coating generated the highest maximum von Mises stress when the displacement of the indenter tip, 7 nm, is applied to all the cases. The table 3 shows the material properties used for the FEA model [8].

Figures 10 (a) through 10 (b) show the contour plots of equivalent plastic strain for different nanocomposite coatings after the nanoindenter tip is removed from the nanocomposite coating surface. Figure 10 (a) illustrates contour plot of the equivalent plastic strain distribution generated inside the YSZ$_{.65}$Au$_{.35}$MoS$_2$ nanocomposite coating. It indicates that the maximum equivalent plain strain occurs in the MoS$_2$ with 8.46 × 10^{-4}. Figure 10 (b) depicts the contour plot of equivalent plastic strain distribution generated inside the YSZ$_{.75}$Au$_{.25}$MoS$_2$ nanocomposite coating. The magnitude of the equivalent plastic strain increases up to 2.30 × 10^{-3} in MoS$_2$ nanocrystalline phase. The area of the permanent deformation increases because the higher modulus of elasticity of YSZ/Au matrix causes higher von Mises stress in YSZ$_{.75}$Au$_{.25}$MoS$_2$ nanocomposite coating. Figure 10 (c) demonstrates the contour plot of equivalent plastic strain distribution generated inside the YSZ$_{.85}$Au$_{.15}$MoS$_2$ nanocomposite coating. The magnitude of the equivalent plastic strain increases up to 2.91 × 10^{-3}. Figure 10 (d) displays the contour plot of equivalent plastic strain distribution generated for YSZ$_{.95}$Au$_{.5}$MoS$_2$ nanocomposite coating. In general, as the modulus of elasticity increases, the magnitude of the von Mises stress generated increases. Therefore, the magnitude of the equivalent plastic strain increases up to 3.48 × 10^{-3}.because of the higher modulus of elasticity of YSZ$_{.95}$Au$_{.5}$MoS$_2$ nanocomposite coating. In addition, as the YSZ composition increase in YSZ/Au amorphous matrix, the larger area below the contact is affected for the plastic deformation, that is, larger permanent plastic deformation area occurs because of the modulus of elasticity and hardness increase.

During the nanoindentation process, the YSZ/Au/MoS$_2$ or YSZ/Au/YSZ coating system still experience the residual stress after the nanoindenter tip is removed from the nanocomposite coating system. Figures 11(a) through 11(d) show the contour plot of residual von Mises stress distribution generated inside the nanocomposite system obtained from the FEA model. As the YSZ composition increases in YSZ/Au matrix, the nanocomposite coating system shows the higher residual von Mises stresses generated inside the coating. Figure 11 (a) depicts the contour plot of residual von Mises stress in YSZ$_{.65}$Au$_{.35}$MoS$_2$ nanocomposite coating after the nanoindentation depth of 7 nm applied and removed from the coating surface. The maximum von Mises stress, 7.26 × 10^7 Pa, is generated below the center of the contact. Figure 11 (b) demonstrates the contour plot of residual von Mises stress distribution inside the YSZ$_{.75}$Au$_{.25}$MoS$_2$ nanocomposite coating. The maximum residual von Mises stress generated below the contact is 2.22 × 10^8 Pa. As the YSZ composition increases in YSZ/Au amorphous matrix, the larger region below the contact surface is influenced by the residual stress under the same loading conditions. Figure 11 (c) illustrates the contour plot of residual stress distribution inside the YSZ$_{.85}$Au$_{.15}$MoS$_2$ nanocomposite coating. The maximum von Mises stress generated below the contact is 3.22 × 10^8 Pa. Figure 11 (d) displays the contour plot of residual von Mises stress distribution inside the YSZ$_{.95}$Au$_{.5}$MoS$_2$ nanocomposite coating. The maximum residual von Mises stress generated below the contact is 4.17 × 10^8 Pa. Larger area of the coating system

6

has the residual von Mises stress inside the nanocomposite coating as the YSZ composition increases.

Figures 12 (a) through 12 (d) show the contour plots of von Mises stress distribution inside the nanocomposite coating system to represent the effect of density of crystalline phase material composition on Von Mises stress. Figure 12 (a) depicts the von Mises stress generated inside $YSZ_{.75}Au_{25}MoS_2$ nanocomposite coating with 75 phase volume % density. Figure 12 (b) displays the von Mises stress generated inside $YSZ_{.75}Au_{.25}MoS_2$ nanocomposite coating with 20 phase volume % density. Because of the lower density (20 %) of the MoS_2 crystalline phase, the higher maximum von Mises stress, $\sigma_{max} = 3.67$ GPa, was generated. Figure 12 (c) demonstrates the von Mises stress distribution generated inside the $YSZ_{.95}Au_{.5}MoS_2$ nanocomposite with 75 phase volume % density. Figure 12 (d) illustrates the von Mises stress distribution generated inside the $YSZ_{.95}Au_{.5}MoS_2$ nanocomposite with 20 phase volume % density. Again, higher maximum von Mises stress, $\sigma_{max} = 5.43$ GPa, was generated in lower density (20 %) nanocomposite coating. In general, higher density (75 %) nanocomposite coating generates lower maximum von Mises stress while the higher density nanocomposite can generate a narrow gap between crystalline grains. Therefore higher volume density nanocomposite is desirable for the same loading conditions.

Figures 13 (a) and 13 (b) show the contour plots of von Mises stress distribution to represent the effect of indenter size on Von Mises stress inside $YSZ_{.75}Au_{.25}MoS_2$ nanocomposite coating system. Figure 13 (a) depicts the von Mises stress distribution in $YSZ_{.75}Au_{.25}MoS_2$ nanocomposite coating system with indenter radius, 7.5 μm, and indenter displacement, 6 nm. The maximum von Mises stress generated is 1.71 GPa under the contact surface. Figure 13 (b) illustrates the von Mises stress in $YSZ_{.75}Au_{.25}MoS_2$ nanocomposite coating system with indenter radius, 15 μm, and displacement, 8 nm. The maximum von Mises stress occurs is 1.64 GPa. Since the area of von Mises stress generated by indentation is significantly influenced by the indenter size, the nanocomposite coating thickness design requires a careful consideration on the indenter size.

Figures 14 (a) through 14 (b) show the contour plots of von Mises stress distribution inside the $YSZ_{.71}Au_{.11}MoS_2$ nanocomposite coating to represent the effect of applied load on von Mises stress. The different indentation depths from 5 nm to 11 nm applied to the nanoindentation simulation for the same contact conditions. Figures 14 (a) and 14 (b) depict the von Mises stress distributions inside the $YSZ_{.71}Au_{.11}MoS_2$ nanocomposite coating for indentation depth, $\delta = 5$ nm and 7 nm. Higher von Mises stress is generated below the contact surface due to the higher displacement, 7nm. Figure 14 (c) shows the von Mises stress inside the $YSZ_{.71}Au_{.11}MoS_2$ nanocomposite coating for indentation depth, $\delta = 9$ nm. Maximum von Mises stress increases up to 2.96 GPa due to the increased indentation depth. Figure 14 (d) depicts the von Mises stress distribution of $YSZ_{71}Au_{11}MoS_2$ nanocomposite coating with $\delta = 11$ nm. In general, as the indenter displacement increases, wider Hertzian contact width and higher von Mises stress occur.

Summary and Conclusion

A FEA model has been developed to investigate the stress distribution and elastic-plastic deformation generated inside the nanocomposite coating system due to the nanoindentation. The concept of Voronoi tessellation was applied to generate the random microgeometries of nanocomposite coatings. In general, YSZ/Au amorphous matrix provided excellent mechanical

properties for contact load support. YSZ/Au coatings with the addition of YSZ crystalline have better load supporting mechanism than YSZ/Au coatings with the addition of MoS_2. The increase of the YSZ composition in YSZ/Au amorphous matrix caused an increase in elastic modulus and subsequent load supporting. Also, the increase of the YSZ composition in YSZ/Au amorphous matrix caused an increase in equivalent plastic strain and subsequent residual stress under the same loading conditions. However, the magnitude of the residual von Mises stress is relatively smaller than the stress generated during the deposition process. The volume density of the crystalline phase material composition plays an important role to maintain the integrity of the coating system because of the material properties and the gap between the crystalline phases. Also, the indenter size effect is significant for nanocomposite coating thickness design. In addition, the applied load is the important operating parameter to design the nanocomposite coating system because the applied load determines coating thickness, crystalline phase density, YSZ/Au composition, and etc.

Acknowledgements

References

[1] A.A. Voevodin, T.A. Fitz, J.J. Hu, and J.S. Zabinski, 2002, "Nanocomposite Tribological Coatings With "Chameleon" Surface Adaptation," J. Vac. Sci. Technol. A 20(4), Jul/Aug 2002, pp. 1434 – 1444.

[2] S. Veprek, M. Haussmann, R. Reiprich, L. Shizhi, and J. Dian, 1996, "Novel Thermodynamically Stable and Oxidation Resistant Superhard Coating Materials," Surf Coat Technol, 86-87, pp. 394-401.

[3] S. Veprek and A.S. Argon, 2001, "Mechanical Properties of Superhard Nanocomposites," Surf Coat Technol, 146-147, pp. 175 – 182.

[4] A.A. Voevodin, J.J. Hu, J.G. Jones, T.A. Fitz, and J.S. Zabinski, 2001, "Growth and Structural Characterization of Yttria-Stabilized Zirconia-Gold Nanocomposite Films with Improved Toughness," Thin Solid Films, 401, pp. 187 – 195.

[5] S. Veprek and A.S. Argon, 2001, "Mechanical Properties of Superhard Nanocomposites," Surf Coat Technol, 146-147, pp. 175 – 182.

[6] S. Veprek and A.S. Argon, 2002, "Towards the Understanding of Mechanical Properties of Super- And Ultrahard Nanocomposites," J. Vac. Sci. Technol. B 20(2). Mar/Apr 2002, pp. 650 – 664.

[7] A.A. Voevodin, J.S. Zabinski, and C. Muratore, 2005, "Recent Adventage in Hard, Tough, and Low Friction Nanocomposite Coatings," Tsinghua Science and Technology, ISSN 1007-0214 02/11 pp. 665-679, Volume 10, Number 6, December 2005.

[8] A.A. Voevodin, J.J. Hu, T.A. Fitz, and J.S. Zabinski, 2001, "Tribological Properties of Adaptive Nanocomposite Coatings Made of Yttira Stabilized Zirconia and Gold," Surf Coat Technol, 146-147, pp. 351-356.

[9] K. Komvopulos, 1988, "Finite Element Analysis of a Layered Elastic Solid in Normal Contact with a Rigid Surface," Journal of Tribology, Vol. 110, pp. 477-485.

[10] K. Komvopulos, 1989, "Elastic-Plastic Finite Element Analysis of Indented Layered Media," Journal of Tribology, Vol. 111, pp. 430-439.

[11] A.K. Bhattacharya and W.D. Nix, 1988, "Analysis of Elastic and Plastic Deformation Associated with Indentation Testing of Thin Films on Substrates," International Journal of Solids and Structures, Vol. 24, No. 12, pp. 1287-1298.

[12] Y. Sun, A. Bloyce, and T. Bell, 1995, "Finite Element Analysis of Plastic Deformation of Various Tin Coating/Substrate Systems Under Normal Contact With A Rigid Sphere," Thin Solid Films, Vol. 271, pp. 122-131.

[13] E.R. Kral and K. Komvopoulos, 1997, "Three-Dimensional Finite Element Analysis of Subsurface Stress and Strain Fields Due to Sliding Contact on an Elastic-Plastic Layered Medium," Journal of Tribology, Vol. 119, pp. 332-341.

[14] N. Ye, and K. Komvopoulos, 2003, "Effect of Residual Stress in Surface Layer on Contact Deformation of Elastic-Plastic Layered Media," Journal of Tribology, Vol. 125, pp. 692-699.

[15] T.Z. Gorishnyy and L.G. Olson, 2003, "Optimization of Wear-Resistant Coating Architectures Using Finite Element Element Analysis," J. Vac. Sci. Technol. A. 21(1), Jan/Feb 2003.

[16] R.G. Veprek, D.M. Parks, A.S. Argon, and S. Veprek, 2006, "Non-linear Finite Element Constitutive Modeling of Mechanical Properties of Hard and Superhard Materials Studied By Indentation," Materials Science and Engineering A 422, pp. 205-217.

[17] S.J. Bull, 1997, Failure modes in the scratch adhesion testing of thin coatings. In: Datta PK, Burnell-Gray JS, editors. Proceedings of the fourth international conference on advances in surface engineering volume 1. Royal Society of Chemistry; pp. 274-85.

[18] S. Weyer, A. Fröhlich, H. Riesch-Oppermann, L. Cizelj, and M. Kovac, 2002, "Automatic Finite Element Meshing of Planar Voronoi Tessellations," Engineering Fracture Mechanics", 69. pp 945-958.

[19] Matlab manual version 6.5.0, 2002.

[20] A.A. Voevodin, S.D. Walck, and J.S. Zabinski, 1997, "Architecture of Multilayer Nanocomposite Coatings with Super-Hard Diamond-Like Carbon Layers for Wear Protection At High Contact Loads", Wear, 203-204 516-527.

Table Captions

Table 1. Mechanical material properties of YSZ/Au/MoS$_2$/DLC composite coatings produced at different deposition temperature [1].

Table 2. Mechanical Material properties of YSZ/Au matrix, YSZ, and MoS2.

Table 3. Mechanical Material properties of YSZ/Au matrix with different amorphous matrix composition properties.

Table 1. Mechanical material properties of YSZ/Au/MoS$_2$/DLC composite coatings produced at different deposition temperature [1].

Coating Designation using molar fractions of the components	Deposition temperature (°C)	Modulus (GPa)	Hardness (GPa)
$(YSZ)_{0.82}(MoS2)_{0.18}$	150	118	10
$(YSZ)_{0.71}Au_{0.11}(MoS2)_{0.18}$	150	47	2
$(YSZ)_{0.58}Au_{0.18}(MoS2)_{0.24}$	300	131	4
$(YSZ)_{0.91}C_{0.09}$	150	173	15
$(YSZ)_{0.78}Au_{0.13}C_{0.09}$	150	66	11
$(YSZ)_{0.81}Au_{0.15}C_{0.04}$	300	187	13
$(YSZ)_{0.45}(MoS2)_{0.33}C_{0.22}$	150	56	5
$(YSZ)_{0.62}(MoS2)_{0.21}C_{0.17}$	300	169	12

Table 2. Material properties of YSZ/Au matrix, YSZ, and MoS2.

Material	Modulus of Elasticity [Pa]	Yield Strength [Pa]
$YSZ_{.71}Au_{.11}$	2.4×10^{11}	5.5×10^{9}
$YSZ_{.58}Au_{.18}$	2.0×10^{11}	3.7×10^{9}
YSZ	3.2×10^{11}	8.3×10^{9}
MoS_2	1.2×10^{11}	1.0×10^{9}

Table 3. Material properties of YSZ/Au matrix with different amorphous matrix composition properties.

Material	Modulus of Elasticity [Pa]	Yield Strength [Pa]
$YSZ_{.95}Au_{.5}$	2.6×10^{11}	7.3×10^{9}
$YSZ_{.85}Au_{.15}$	2.3×10^{11}	5.3×10^{9}
$YSZ_{.75}Au_{.25}$	2.0×10^{11}	3.7×10^{9}
$YSZ_{.65}Au_{.35}$	1.5×10^{11}	2.8×10^{9}

(a)

(b)
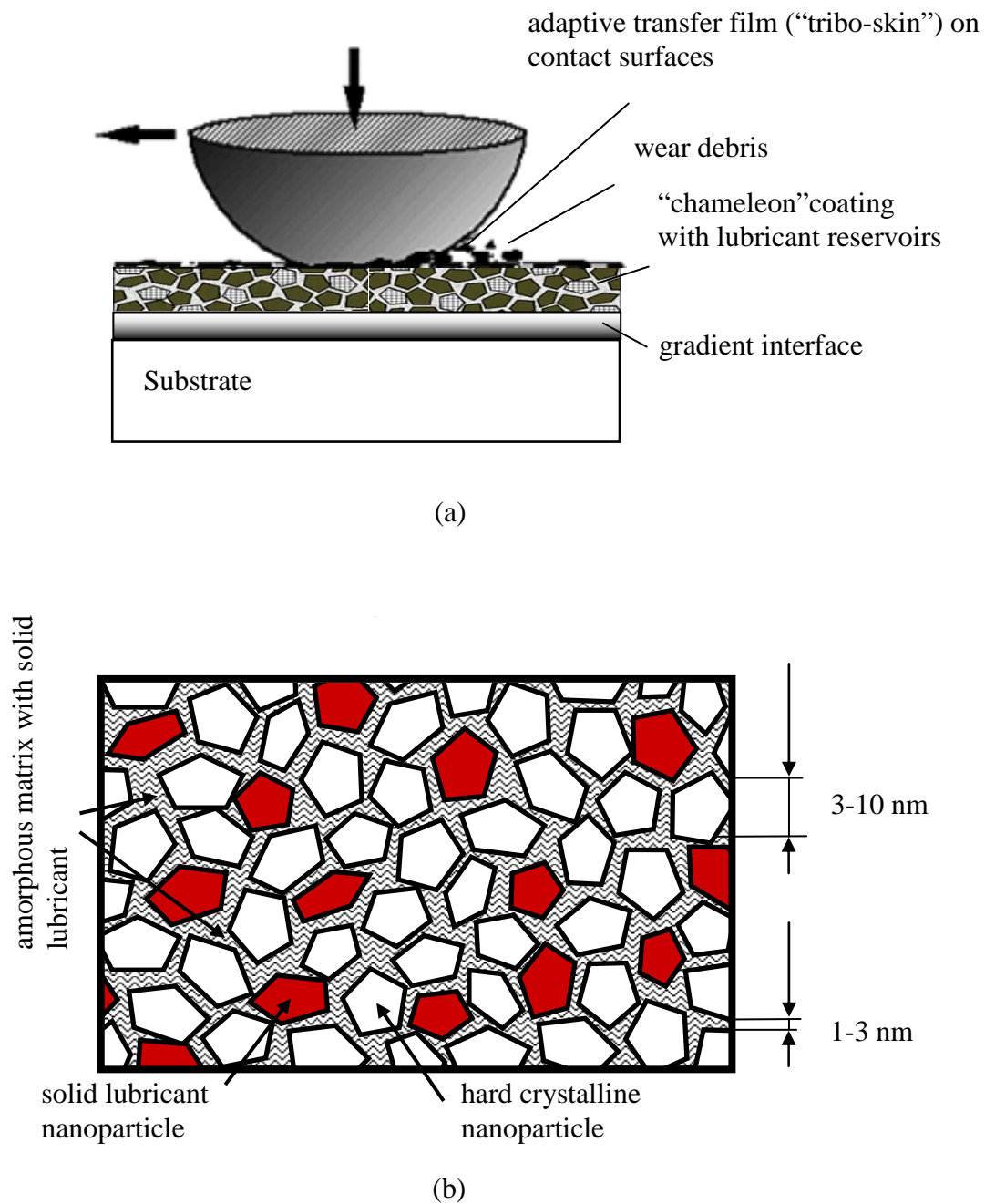
Figure 1. (a) Schematic of nanocomposite coating system, featuring a crystalline/amorphous design in the main coating layer for cohesive toughness and a functionally gradient interface layer for adhesive toughness; (b) Schematic of nanocomposite coating design structure, that is, an amorphous matrix and crystalline phase (YSZ) were used for an optimum mechanical performance and load support.
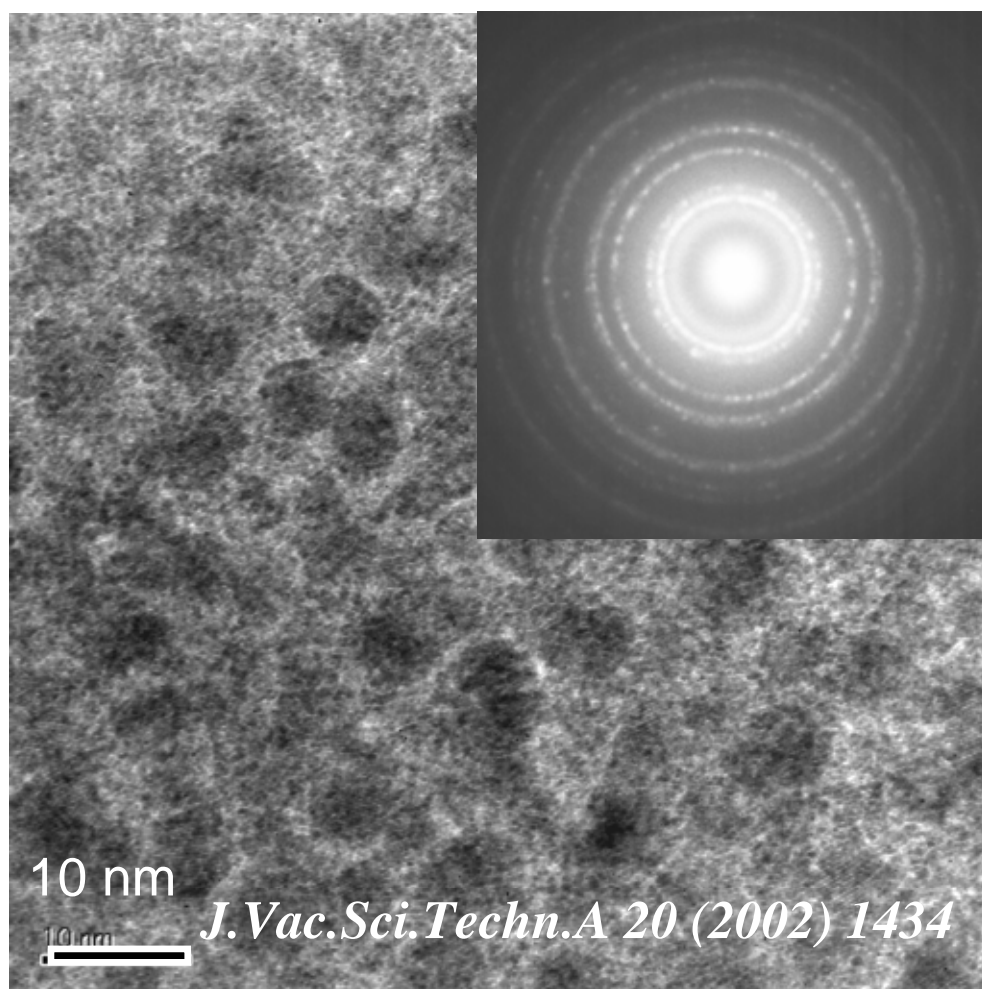
Figure 2. HRTEM (high resolution transmission electron microscope) image and SAD (submicron selected area electron diffraction) pattern obtained from $(YSZ)_{0.48}$ $Au_{0.12}$ $(MoS_2)_{0.18}$ $C_{0.22}$, that is, an example of "Chameleon" nanostructure, i.e. YSZ/Au/MoS$_2$/DLC nanocomposite coating produced by a hybrid of laser ablation and magnetron sputtering [1].

(a)

(b)
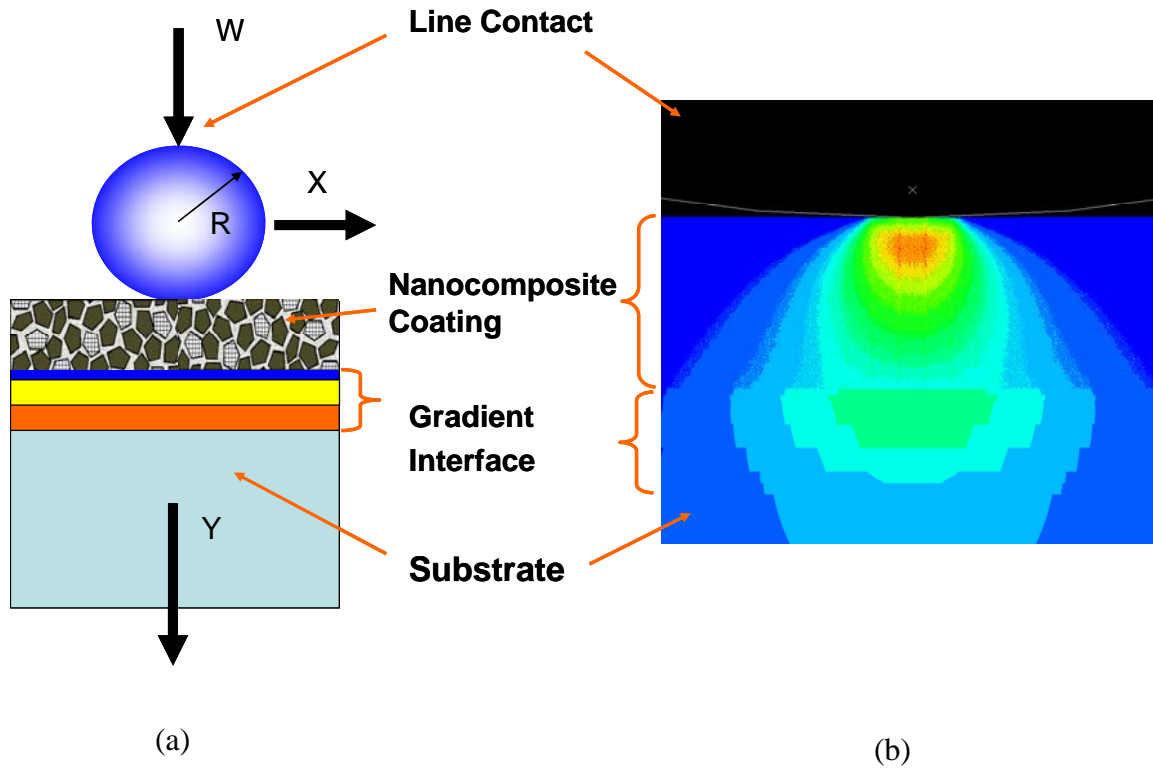
Figure 3. (a) Schematic of line contact for nanocomposite coating system; (b) Finite element analysis model for nanoindentation of nanocomposite coating system.
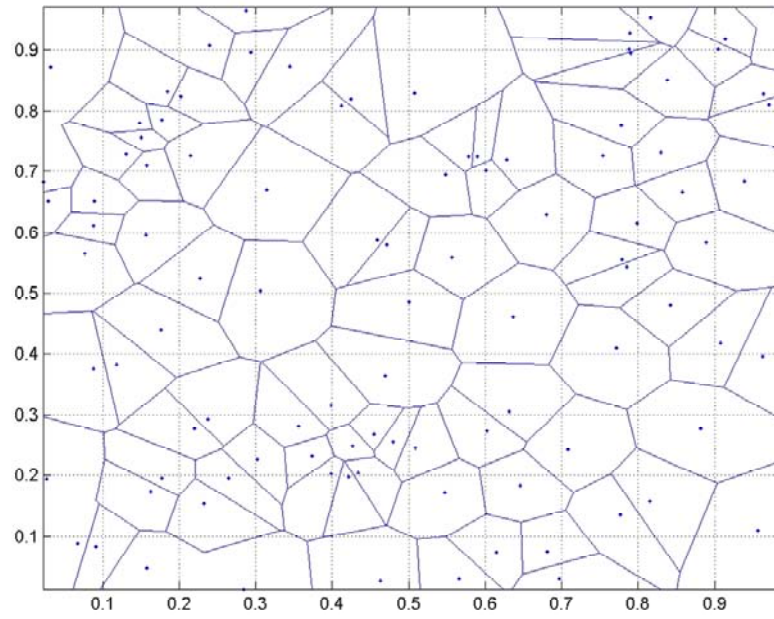
(a)
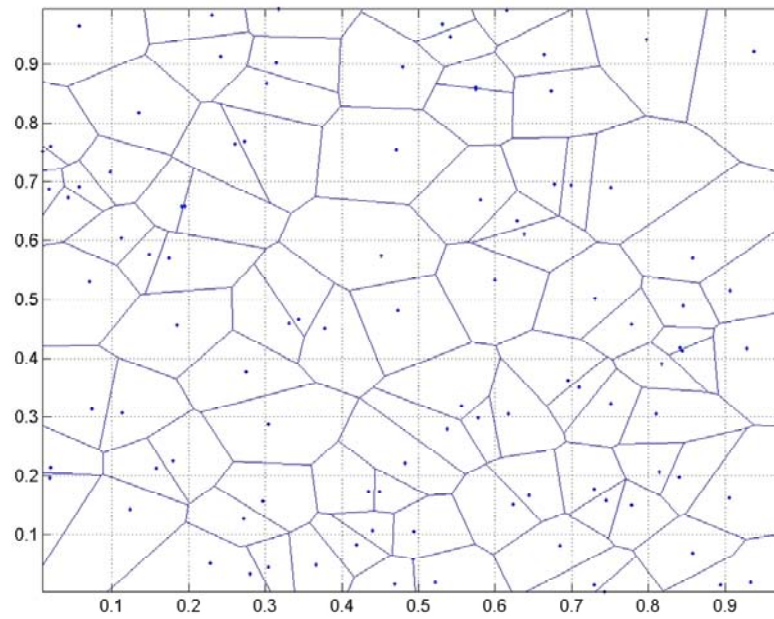
(b)

Figure 4. Schematic of random microstructure geometries generated based on the concept of Voronoi tessellation; (a) 75th state; (b) 50th state.
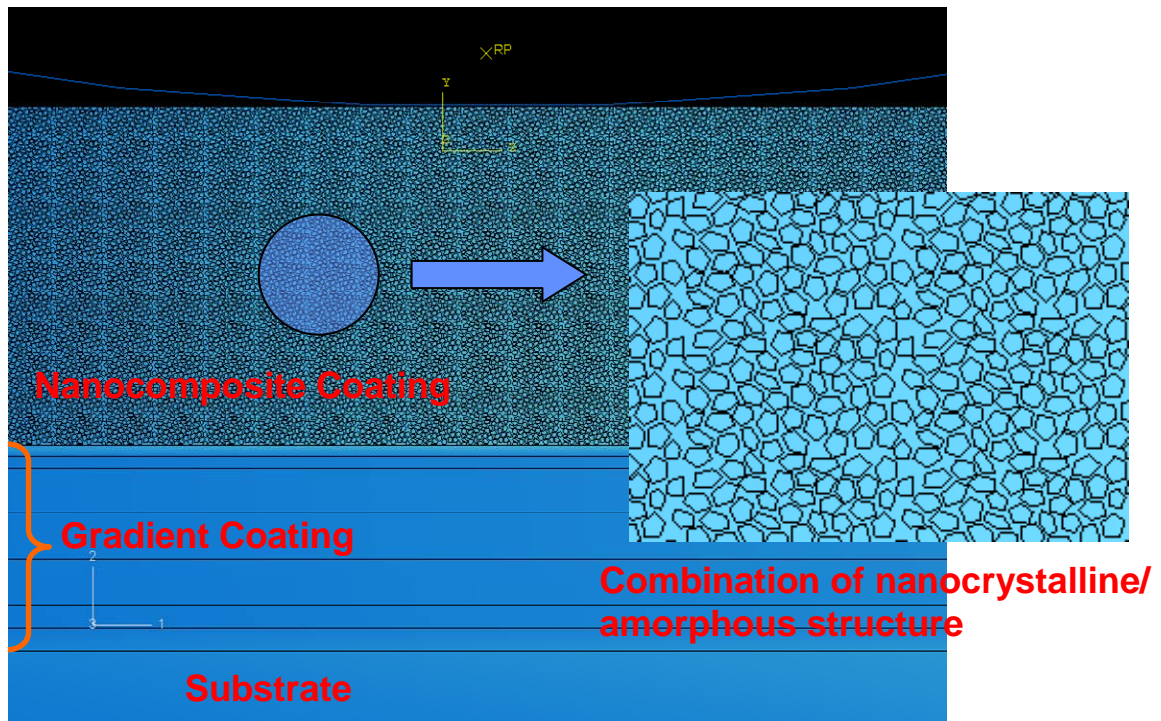
Figure 5. Finite element analysis model of nanocomposite coating system nanoindentation.
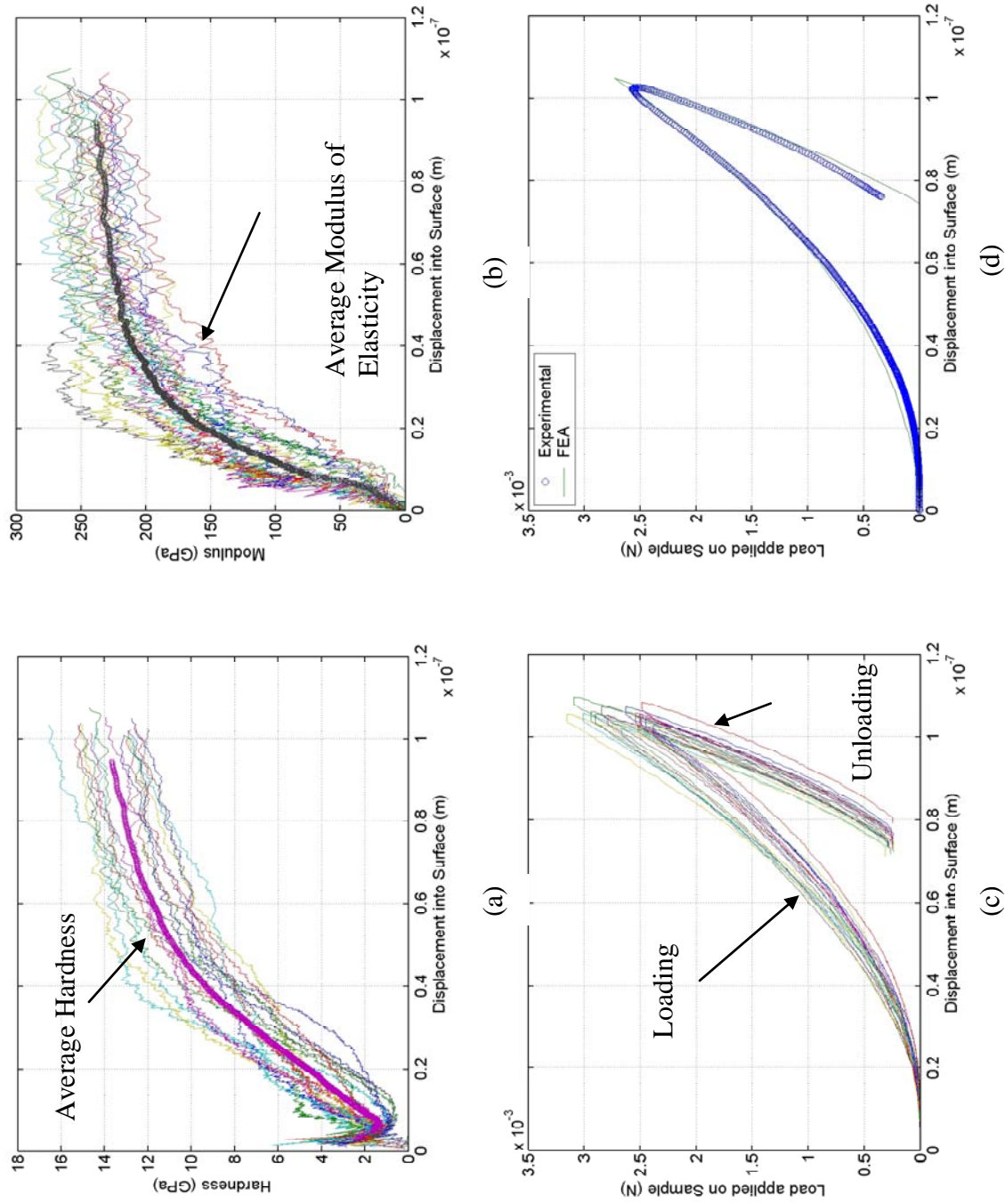
Figure 6. Nanoindentation results for Ti$_{.53}$C$_{.47}$ coating; (a) hardness vs. displacement plot, (b) modulus of elasticity vs displacement plot, (c) load vs. displacement plot during loading and unloading stages, and (d) comparison of measured average load vs. displacement curve and best-fit load vs. displacement curve from experiments and FEA simulations, respectively.

Material	H	E	Y	Thickness	Poisson's Ratio
Ti$_{.10}$C$_{.90}$	14 GPa	180 GPa	9 GPa	25 nm	0.15
Ti$_{.25}$C$_{.75}$	21 GPa	260 GPa	14 GPa	25 nm	0.15
Ti$_{.30}$C$_{.70}$	24 GPa	290 GPa	16 GPa	100 nm	0.20
Ti$_{.50}$C$_{.50}$	15 GPa	250 GPa	10 GPa	100 nm	0.20
Ti$_{.70}$C$_{.30}$	11 GPa	200 GPa	7.5 GPa	100 nm	0.25
Ti$_{.90}$C$_{.10}$	5 GPa	145 GPa	2.5 GPa	50 nm	0.25
α-Ti	2 GPa	136 GPa	1.5 GPa	50 nm	0.25
440C steel	9 GPa	220 GPa	4 GPa		0.30

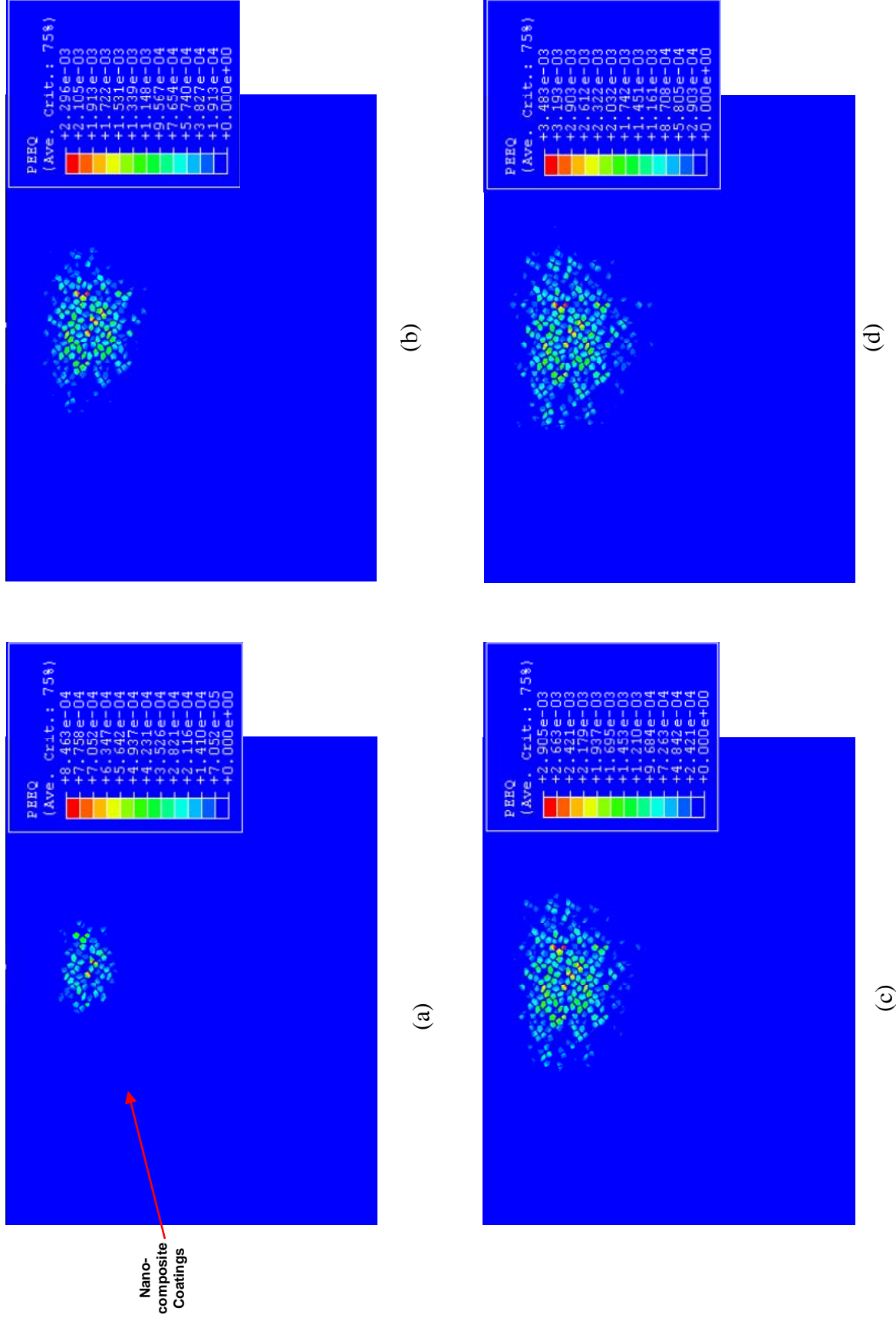Figure 7 Schematic of functionally gradient Ti/TiC Interface Design
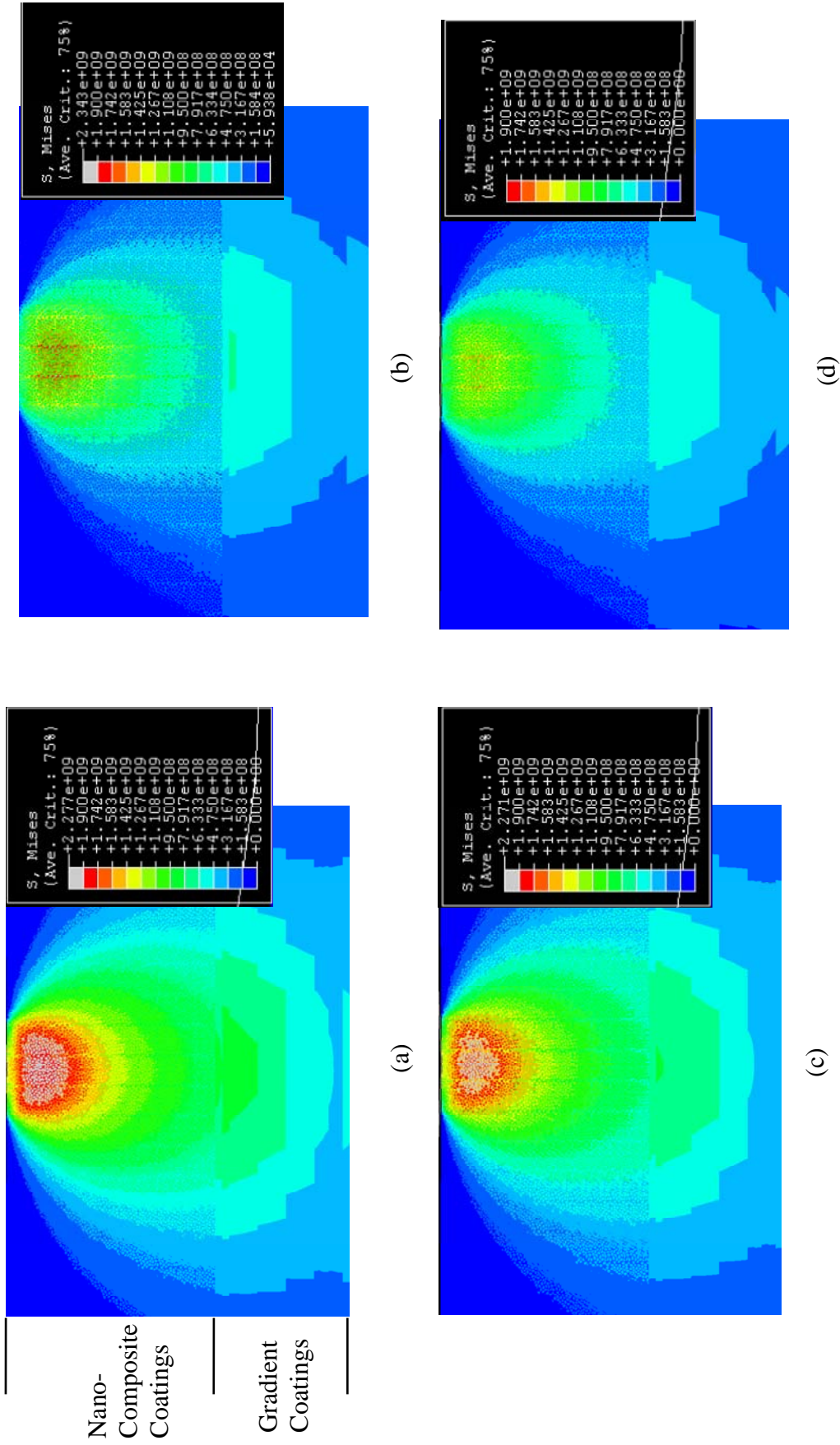
Figure 8. Contour plots of von Mises stresses distribution generated inside the nanocomposite coating system from the FEA model with different crystalline properties at indentation depth, $\delta = 7$ nm: (a) $YSZ_{.71}Au_{.11}YSZ$; (b) $YSZ_{.71}Au_{.11}MoS_2$; (c) $YSZ_{.58}Au_{.18}YSZ$; and (d) $YSZ_{.58}Au_{.18}MoS_2$.
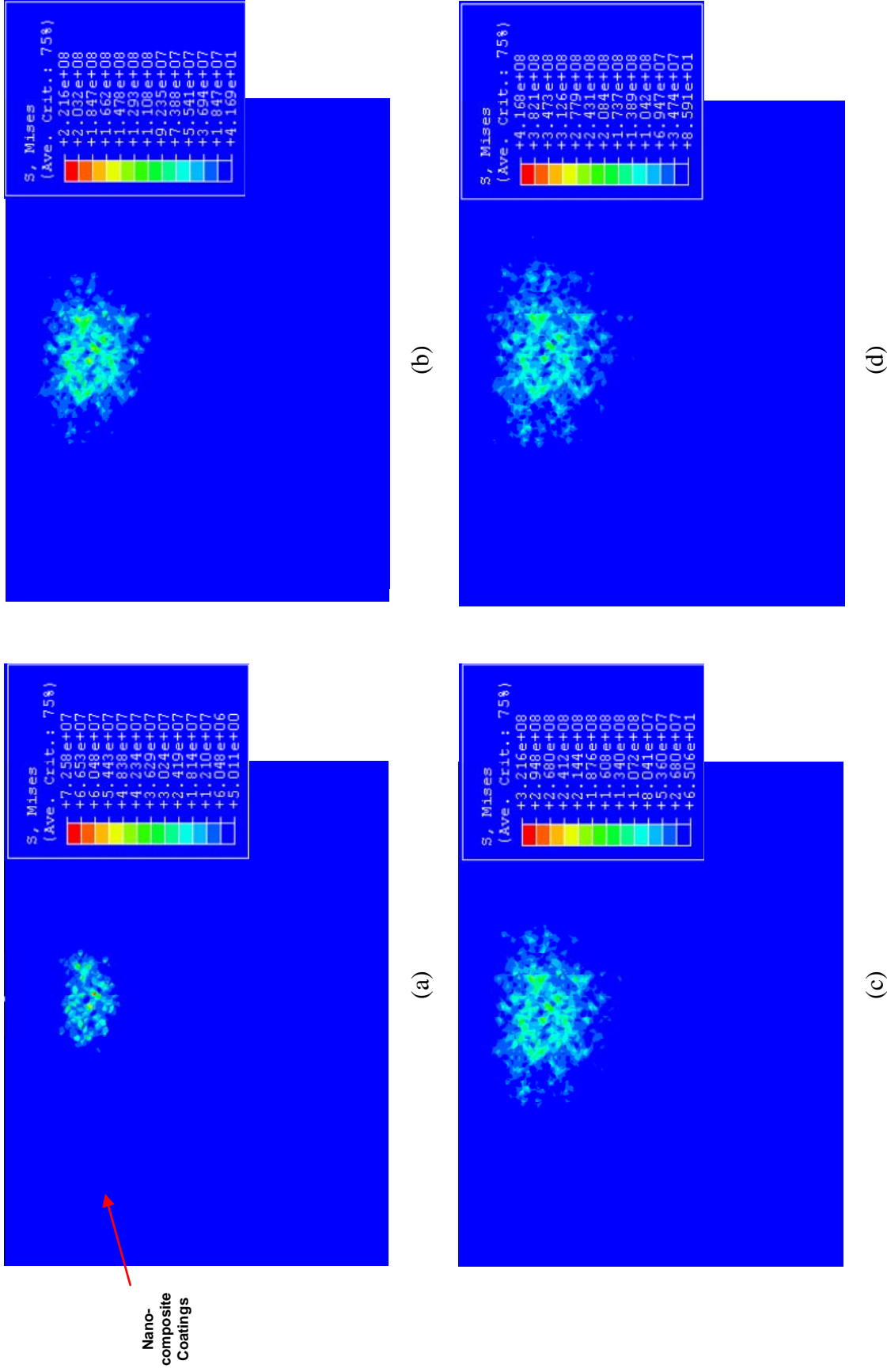
Figure 9. Contour plots of von Mises stresses distribution generated inside the nanocomposite coating system from the FEA model with different amorphous matrix composition properties at indentation depth, $\delta = 7$ nm: (a) $YSZ_{.65}Au_{.35}MoS_2$, σ_{max} =1.27 GPa; (b) $YSZ_{.75}Au_{.25}MoS_2$, σ_{max} = 1.83 GPa; (c) $YSZ_{.85}AU_{.15}MoS_2$, σ_{max} = 2.22 GPa; and (d) $YSZ_{.95}Au_{.5}MoS_2$, σ_{max} = 2.59 GPa.
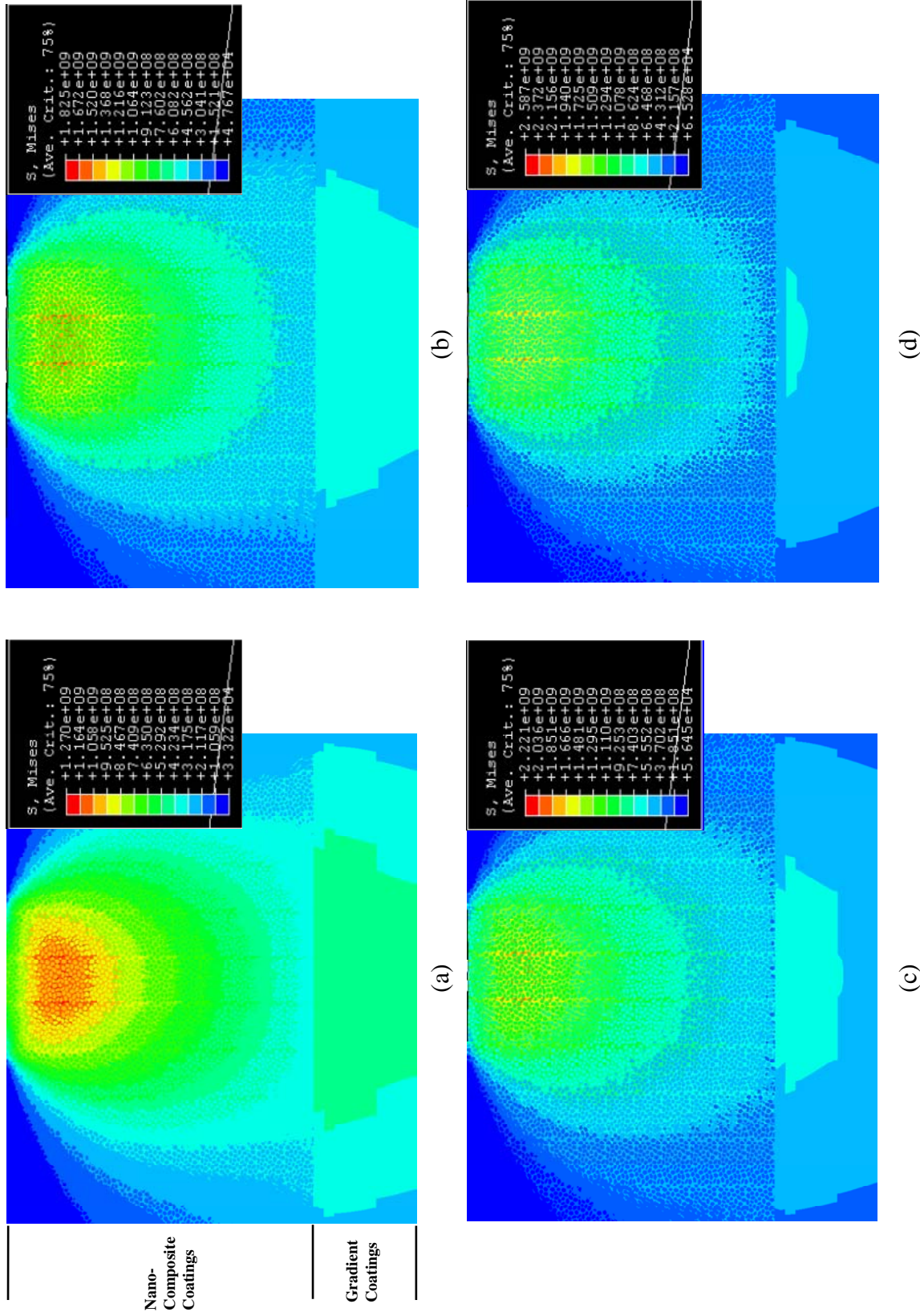
Figure 10. Contour plots of equivalent plastic strain distribution generated inside the nanocomposite coating system from the FEA model with different amorphous matrix composition properties at indentation depth, $\delta = 7$ nm: (a) $YSZ_{.65}Au_{.35}MoS_2$, 8.46 $\times 10^{-4}$; (b) $YSZ_{.75}Au_{.25}MoS_2$, 2.30 $\times 10^{-3}$; (c) $YSZ_{.85}AU_{.15}MoS_2$, 2.91 $\times 10^{-3}$; (d) $YSZ_{.95}Au_{.5}MoS_2$, 3.48 $\times 10^{-3}$.
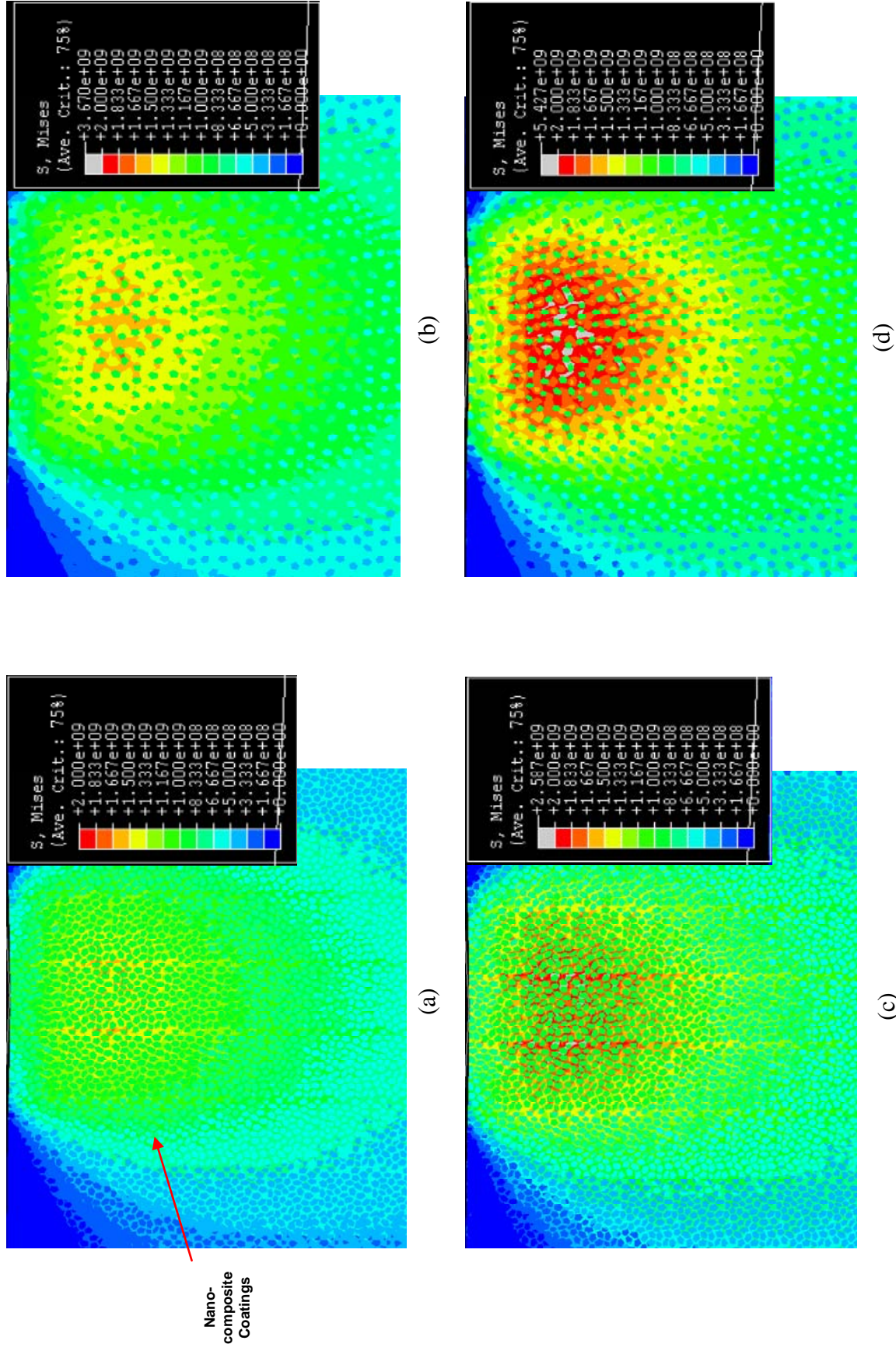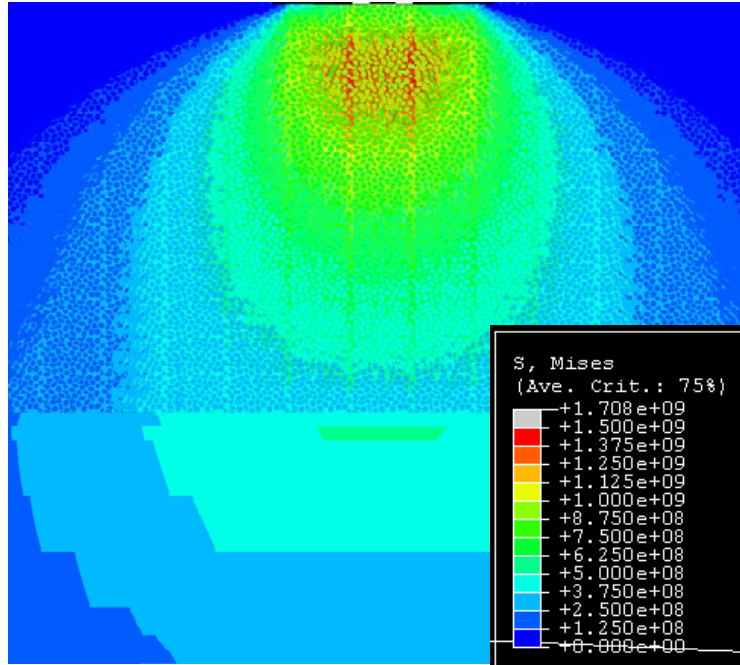
Figure 11. Contour plots of residual von Mises stress distribution generated inside the nanocomposite coating system from the FEA model with different amorphous matrix composition properties at indentation depth, $\delta = 7$ nm: (a) $YSZ_{.65}Au_{.35}MoS_2$, 7.26×10^7 Pa; (b) $YSZ_{.75}Au_{.25}MoS_2$, 2.216×10^8 Pa ; (c) $YSZ_{.85}AU_{.15}MoS_2$, 3.22×10^8 Pa; (d) $YSZ_{.95}Au_{.5}MoS_2$, 4.17×10^8 Pa.
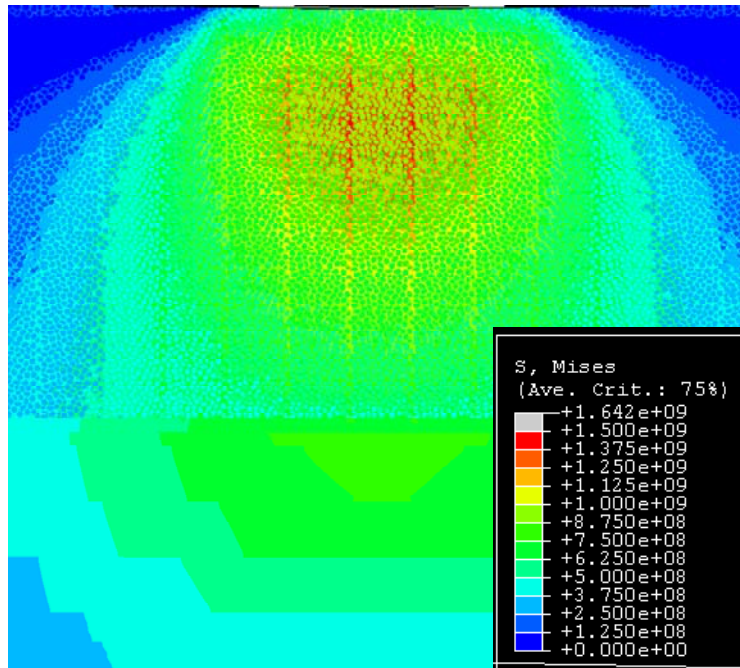
23

Figure 12. Contour plots of von Mises stress distribution generated inside the nanocomposite coating system from the FEA model with different matrix/inclusion material composition at indentation depth, $\delta = 7$ nm: (a) $YSZ_{.75}Au_{.25}MoS_2$, $\sigma_{max} = 1.83$ GPa; (b) $YSZ_{.75}Au_{.25}MoS_2$, $\sigma_{max} = 3.67$ GPa; (c) $YSZ_{.95}AU_{.5}MoS_2$, $\sigma_{max} = 2.59$ GPa; (d) $YSZ_{.95}Au_{.5}MoS_2$, $\sigma_{max} = 5.43$ GPa.

(a)

(b)

Figure 13. Contour plots of von Mises stress distribution generated inside the nanocomposite coating system from the FEA model with different indenter radius and indentation depth (a) YSZ$_{.75}$Au$_{.25}$MoS$_2$, R = 7.5 μm, δ = 6 nm; (b) YSZ$_{.75}$Au$_{.25}$MoS$_2$, R = 15 μm, δ = 8 nm.
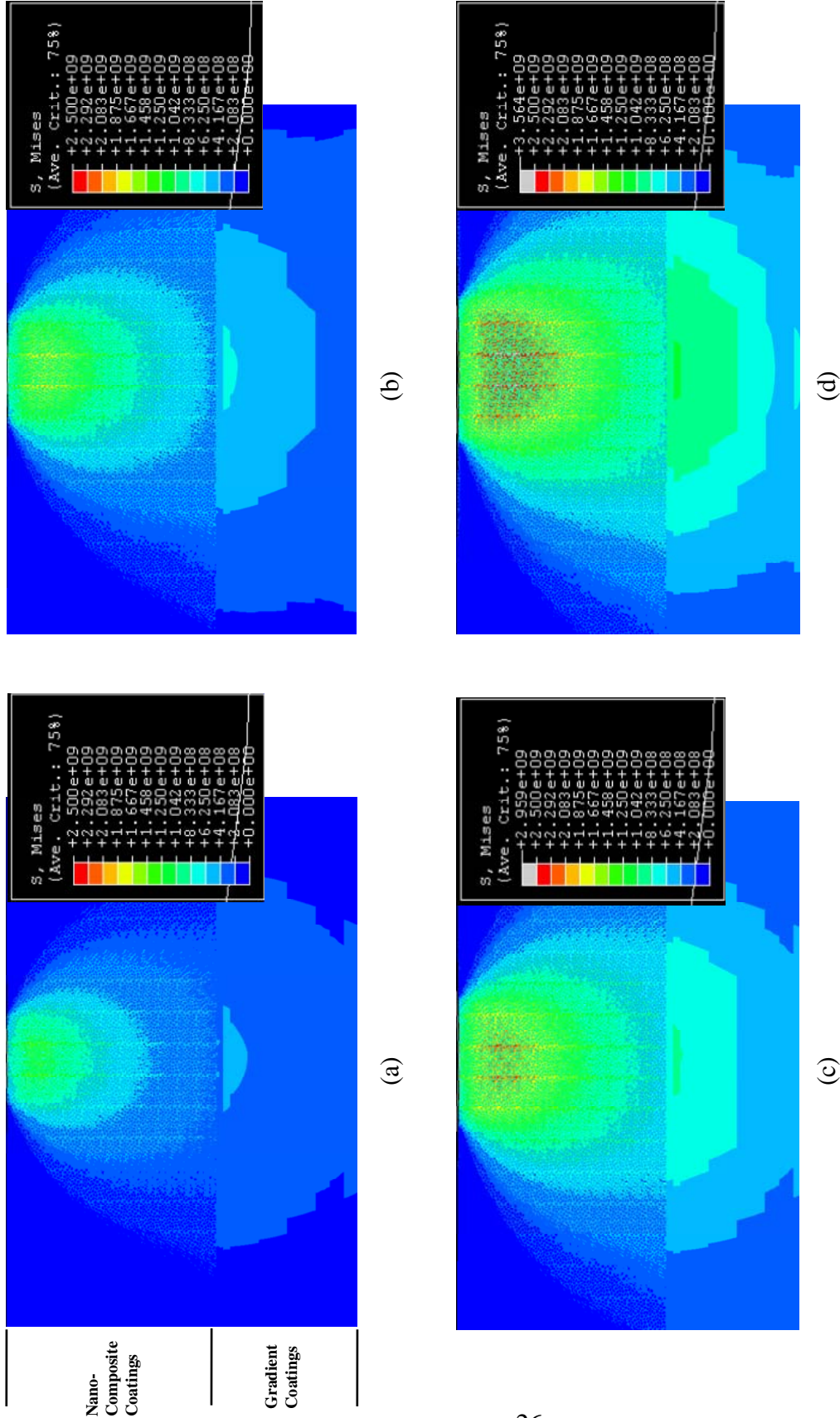
Figure 14. Contour plots of von Mises stress distribution generated inside the $YSZ_{.71}Au_{.11}MoS_2$ nanocomposite coating system from the FEA model at different indentation depths, $\delta = 7$ nm: (a) $\delta = 5$ nm; (b) $\delta = 7$ nm; (c) $\delta = 9$ nm; (d) $\delta = 11$ nm.

26